crystals

MDPI

Review

Insights into Solution Structures of Photosynthetic Protein Complexes from Small-Angle Scattering Methods

Maksym Golub [1], Adrian Kölsch [2], Artem Feoktystov [3], Athina Zouni [2] and Jörg Pieper [1,*]

1 Institute of Physics, University of Tartu, Wilhelm Ostwaldi 1, 50411 Tartu, Estonia; maksym.golub@ut.ee
2 Department of Biology, Humboldt Universität zu Berlin, Philipp Str. 13, 10115 Berlin, Germany; adrian.koelsch@googlemail.com (A.K.); athina.zouni@hu-berlin.de (A.Z.)
3 Forschungszentrum Jülich GmbH, Jülich Centre for Neutron Science (JCNS) at Heinz Maier-Leibnitz Zentrum (MLZ), Lichtenbergstr. 1, 85748 Garching, Germany; a.feoktystov@fz-juelich.de
* Correspondence: pieper@ut.ee

Abstract: High-resolution structures of photosynthetic pigment–protein complexes are often determined using crystallography or cryo-electron microscopy (cryo-EM), which are restricted to the use of protein crystals or to low temperatures, respectively. However, functional studies and biotechnological applications of photosystems necessitate the use of proteins isolated in aqueous solution, so that the relevance of high-resolution structures has to be independently verified. In this regard, small-angle neutron and X-ray scattering (SANS and SAXS, respectively) can serve as the missing link because of their capability to provide structural information for proteins in aqueous solution at physiological temperatures. In the present review, we discuss the principles and prototypical applications of SANS and SAXS using the photosynthetic pigment–protein complexes phycocyanin (PC) and Photosystem I (PSI) as model systems for a water-soluble and for a membrane protein, respectively. For example, the solution structure of PSI was studied using SAXS and SANS with contrast matching. A Guinier analysis reveals that PSI in solution is virtually free of aggregation and characterized by a radius of gyration of about 75 Å. The latter value is about 10% larger than expected from the crystal structure. This is corroborated by an ab initio structure reconstitution, which also shows a slight expansion of Photosystem I in buffer solution at room temperature. In part, this may be due to conformational states accessible by thermally activated protein dynamics in solution at physiological temperatures. The size of the detergent belt is derived by comparison with SANS measurements without detergent match, revealing a monolayer of detergent molecules under proper solubilization conditions.

Keywords: small-angle neutron scattering; Photosystem I; solution structure; detergent belt

Citation: Golub, M.; Kölsch, A.; Feoktystov, A.; Zouni, A.; Pieper, J. Insights into Solution Structures of Photosynthetic Protein Complexes from Small-Angle Scattering Methods. *Crystals* **2021**, *11*, 203. https://doi.org/10.3390/cryst11020203

Academic Editor: Oliviero Carugo

Received: 31 January 2021
Accepted: 16 February 2021
Published: 19 February 2021

1. Introduction

A proper understanding of protein function requires detailed knowledge about the three-dimensional static protein structure. One prototypical example is photosynthesis, a vital physiological process converting solar radiation into storable chemical energy [1], which takes place mainly in membrane-bound pigment–protein complexes (photosystems) found in higher plants, algae, and cyanobacteria. Photosystem II (PSII) acts as a light-triggered water: plastoquinone oxidoreductase splitting water into dioxygen, protons, and electrons, which are eventually transferred to plastocyanin [2–4]. Photosystem I (PSI) is a large pigment–protein complex catalyzing electron transfer from reduced plastocyanin or cytochrome *c6* to ferredoxin, resulting in the production of energy-rich stands for nicotinamide adenine dinucleotide phosphate hydrogen (NADPH) [1,5]. PSI is also an attractive system for biotechnological applications [6–9].

For a long time, high-resolution structures of PSI have been obtained using electron crystallography at cryogenic temperatures, e.g., for PSI of *Thermosynechococcus elongatus* (*T. elongatus*) [10] and for plant PSI [11]. More recently, the emergence of femtosecond serial

crystallography using X-ray free electron laser (XFEL) opened up the opportunity to determine the crystal structures of PSI [12] and PSII core complexes [13] at room temperature. In the case of PSII, an expansion of the protein in the order of about ~0.5 Å in all directions was reported at physiological temperatures [13]. In addition, the structures of PSII in all four metastable intermediate S-states of the Kok cycle were determined using XFEL crystallography under physiological conditions [14]. More recently, a high-resolution structure of PSI became available from cryo-electron microscopy (cryo-EM) experiments [15], which also revealed deviations from crystal structures in the form of an expansion of PSI in solution. This means that the low-temperature crystal structure of a photosystem may differ from physiological conditions at room temperature (as demonstrated by XFEL crystallography) but also from those in solution state (as demonstrated by cryo-EM).

While the high-resolution methods for protein structure determination discussed above are restricted either to low temperatures or to the use of protein crystals, functional studies and biotechnological applications of photosystems require proper isolation of the protein in aqueous solution. As a transmembrane protein, however, PSI can only be extracted by solubilization using amphipathic detergent molecules. As a result, the isolated protein is surrounded by a detergent belt in buffer solution, which is not discernible in crystal structures because of its significant structural heterogeneity. Therefore, the general relevance of the high-resolution structures for solubilized PSI has to be independently verified, because the protein structure may generally deviate from its crystal structure in buffer solution at physiological temperatures [16–19].

In this regard, small-angle neutron and X-ray scattering (SANS and SAXS, respectively) become the missing link by providing structural information on proteins in aqueous solution at physiological temperatures [20–22], including membrane proteins solubilized using detergent molecules [21]. In turn, conformational dynamics [23,24] as well as vibrational properties of biomolecules [25,26] may be studied by neutron spectroscopy. SANS and SAXS have already been applied in photosynthesis research (see [27,28] for reviews). SANS can be used, e.g., to investigate lateral spacings of membrane stacks [29–32]. In addition, SANS is also employed to determine low-resolution solution structures of photosynthetic pigment–protein complexes [19,33–39].

In the present contribution, we review selected prototypical applications of SAXS and SANS to photosynthetic pigment–protein complexes using PSI as the major example. We first provide a concise overview about the most necessary theory of SAXS and SANS. The following main part of this short review is divided into three subsections: (i) SAXS data of the water-soluble complex phycocyanin (PC) are used to determine the oligomerization state and the solution structure of a protein, (ii) SAXS data of PSI demonstrate the additional complexity encountered in the case of a the membrane protein, and (iii) SANS data of PSI illustrate the principle of contrast variation in investigations of the solution structure of a membrane protein and of its detergent belt.

2. Basic SANS/SAXS Theory

Theoretical background: SANS and SAXS are complementary experimental techniques allowing to measure the form factor $P(Q)$ representing size and shape of a biomolecule in aqueous solution at physiological temperatures as a function of the scattering vector Q [20,22]. The latter is related to the scattering angle 2θ and to the wavelength of the incident quasi-monochromatic radiation λ_0 by the relation

$$Q = \frac{4\pi}{\lambda_0} \sin(\theta), \tag{1}$$

Then, the intensity measured in a SANS experiment as a function of the scattering vector Q is related to the form factor $P(Q)$ by the master equation [20,22]

$$I(Q) = n\Delta\rho^2 V^2 P(Q) S(Q), \tag{2}$$

where n is the particle number density, $\Delta\rho$ is the difference in scattering length density (SLD) between the particles and the solvent defining the contrast, and V is the volume of the particles. The effective structure factor $S(Q)$ is assumed to be equal to unity in the case of a diluted solution of monodisperse particles.

A model-independent analysis of small-angle scattering data can be performed according to the classical Guinier approximation valid for diluted solutions of monodisperse particles and at small Q values satisfying the condition $QR_g < 1.3$ [40]. This approximation leads to a relatively simple relation between the measured intensity and the radius of gyration according to

$$I(Q) = I(0) \exp\left(-Q^2 \frac{R_g^2}{3}\right), \tag{3}$$

where Q is the scalar value of the scattering vector, R_g is the radius of gyration, and $I(0)$ is the forward scattering, which is a shape independent function of the total scattering power of the sample.

The scattered intensity can also be related to a function $P(R)$ describing the distribution of pair distances of all atoms in a biomolecule. In the case of monodisperse macromolecular solutions, the scattering intensity is proportional to the scattering of a single particle averaged over all orientations, given by a Fourier transformation following

$$I(Q) = 4\pi \int_0^{D_{\max}} P(R) \frac{\sin(QR)}{QR} dR, \tag{4}$$

where $P(R)$ is the pair distance distribution function and $D_{\max}$ corresponds to the maximum distance in the particle. The $P(R)$ function and the particle maximum dimension $D_{\max}$ can be determined using the inverse Fourier transform (IFT) method employing the software routine Gnom [41].

Further data analysis can be carried out using dedicated software packages developed by the group of Dr. Dmitri Svergun [42–44]. The overall shape of a molecule could be reconstructed from its P(R) function using the Dammif program, which is based on a reverse Monte Carlo minimization approach [42,43]. Furthermore, an application of the Cryson/Crysol programs [45,46] allows calculation of theoretical SANS/SAXS curves based on a pdb structure for comparison with the experimental SANS/SAXS data. One can use Pymol program [47] to visualize and compare the results of the Dammif analysis with the known pdb structure of a given protein complex.

While both SANS and SAXS techniques provide information about the size and shape of biomolecules, their nature of interaction with a sample is different. Neutrons interact with the nuclei of a biomolecule, while X-rays get scattered by electrons. Due to the sensitivity of neutrons for different isotopes of the same atom, SANS has the special advantage of contrast variation by isotope exchange, e.g., the replacement of hydrogens by deuterium. Therefore, SANS is a useful tool to study multicomponent protein complexes with selective deuterium labeling of individual components. Moreover, SANS is a powerful technique to probe systems containing components with different scattering length densities, e.g., lipid (or detergent)–protein systems. The structural information of each individual component can be probed by varying the D_2O ratio in the solvent referred to as contrast variation or scattering length density matching. For example, the match points for lipids/detergents, proteins, and nucleic acids are 5–25%, 40–45%, and 65–70% of D_2O, respectively [48].

Although SAXS (almost) does not permit contrast variation, because isotopes like hydrogen and deuterium have the same X-ray scattering length, SAXS has considerable advantages in other respects. SAXS instruments are more widely available for practical use, and their photon flux is several orders of magnitude higher than that of SANS instruments. Despite the risk of radiation damage occurring in SAXS experiments, the small amount of sample required and short measurement time in comparison to SANS experiments make this technique quite attractive to study biological systems. According to the statistics of the

Small Angle Biological Data Bank (SASBDB), 93% of deposited SAS entries were measured on synchrotron radiation facilities, and only 2% were obtained using neutrons [49]. Table 1 compares some basic features of SANS and SAXS from a practical point of view.

Table 1. Practical comparison of small-angle neutron and X-ray scattering (SANS and SAXS, respectively) methods (information is taken from [36]). For ease of inspection, the SANS entries are shown with light grey background.

	SANS	**SAXS**
Incident beam source	Neutrons	Photons (X-ray)
Interacting field	Nuclei	Electrons
Incident beam wavelength (Å)	4–25	1–1.5
Incident beam flux	10^8–10^9 neutrons/cm^2/s	10^{11} photons/cm^2/s
Typical sample counting time	Minutes to hours	Seconds to minutes
Contrast variation	Yes	No
Radiation damage	No	High (synchrotron radiation)
Sample amount required	High	Medium
Availability	Large facility only	Laboratory and synchrotron radiation sources

SANS experiments: In order to achieve an appropriate comparison of SAXS and SANS data of PSI, i.e., for one and the same membrane protein, we include unpublished SANS data for PSI in 100% D_2O. The corresponding SANS experiments on PSI were performed at the KWS-1 small-angle diffractometer (JCNS at MLZ, Garching, Germany) [50,51]. The neutron wavelength used in this experiment was 5 Å with 10% wavelength spread. The accessible range of the scattering vector Q was extended from 0.006 to 0.45 Å^{-1} by measuring at two sample-detector distances of 8 and 20 m, respectively. The purification of PSI from *T. elongatus* was performed as described earlier [15,52,53] so that the results are directly comparable to [15].

2.1. SANS/SAXS DATA of Photosynthetic Protein Complexes

2.1.1. PC as Example for a Water-Soluble Protein Studied by SAXS

A prototypical application for SANS/SAXS is the study of oligomerization states of proteins in aqueous solutions. As an example, we briefly discuss the case of the light-harvesting complex phycocyanin (PC) from *T. elongatus*, which may occur in trimeric or hexameric form—see crystal structures with PDB codes 4ZIZ [54] and 4Z8K [55], respectively. PC is a pigment–protein complex binding nine bilin chromophores per trimer and an important constituent of various cyanobacterial antenna [56,57]. It is thus involved in efficient light-harvesting and excitation energy transfer to reaction center complexes in cyanobacteria [58–60]. SAXS data of PC from *T. elongatus* in solution are shown in Panel A of Figure 1 (data taken from Golub et al., 2017 [61]). The software package CRYSOL allows computing SAXS curves directly from the PDB codes of the trimeric and hexameric PC structures represented by the full black and red lines in Panel A, respectively. It is apparent that the data can be very well described by the trimeric form of PC. In contrast, the SAXS curve generated for the hexameric structure is shifted toward lower values of the scattering vector q and, thus, appears to be too large to fit the data of the sample under study. Furthermore, an ab initio shape reconstitution of PC was performed based on the SAXS data using the reverse Monte Carlo approach available using the ATSAS software routine. The corresponding low-resolution model of PC is depicted by grey spheres in Figure 1 and compared to the high-resolution crystal structure of PC. A comparison reveals that the low-resolution structure also compares well to the trimeric form of PC and yields a disk-shaped structure with a height and a diameter of roughly 28 Å and 100 Å, respectively.

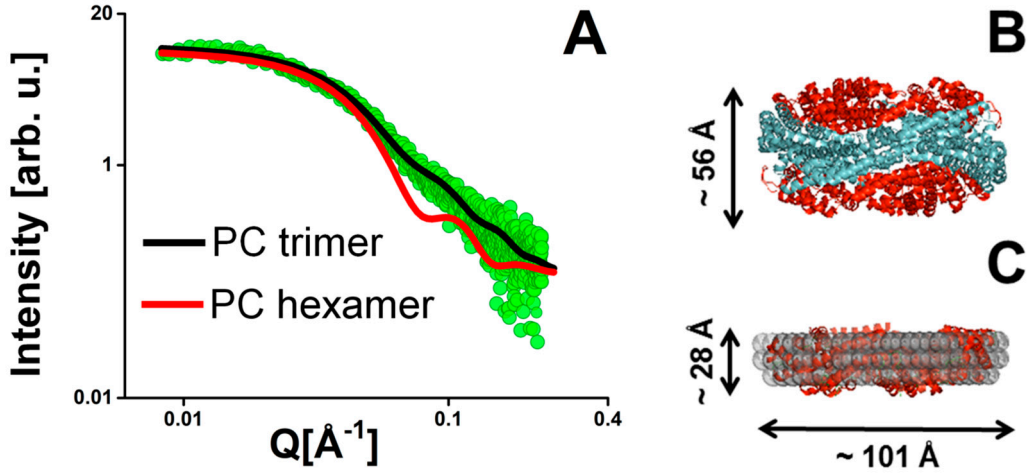

Figure 1. Panel (**A**): SAXS data of phycocyanin (PC) from *T. elongatus* obtained on Nanostar (green circles) at room temperature. The full black and red lines are fits based on the structures trimeric (black line) and hexameric PC (red line) using the program package CRYSOL. Panel (**B**): Crystal structure of PC from *T. elongatus* in hexameric form based on PDB code 4ZIZ [54]. Panel (**C**) Crystal structure of PC from *T. elongatus* in trimeric form based on PDB code 4Z8K [55]. The grey spheres in Panel C show the low-resolution structure of PC obtained using the program ATSAS from the SAXS data shown in Panel (**A**). Graphics taken from Golub et al. BBA 2017 [61] with permission.

2.1.2. PSI as Example for a Membrane Protein Studied by SAXS

Above, we have mainly discussed applications of SANS/SAXS in studies of water-soluble (photosynthetic) proteins. In such cases, SANS and SAXS can be used almost analogously. The situation is much more complex when considering membrane proteins that have to be solubilized in detergents to achieve aqueous solutions.

As an example, SAXS data of monomeric and trimeric photosystem I (PSI) of *T. elongatus* are shown in Figure 2 (data taken from Golub et al. [62]). The data obtained in the region of small scattering vectors q are depicted in the upper panel of Figure 2 in the form of a Guinier plot. Both forms of PSI reveal a linear behavior as expected in the absence of aggregation but exhibit different slopes corresponding to radii of gyration of 58 and 78 Å in the cases of monomeric and trimeric PSI, respectively. That is, similar to the case of PC discussed above, the oligomerization state of PSI can be investigated by SAXS.

The lower Panel of Figure 2 compares SAXS data of monomeric PSI with a curve simulated based on the crystal structure of monomeric PSI (pdb code 1JB0, Jordan et al., 2001), see green line. In contrast to the case of PC presented above, the SAXS curve calculated from the crystal structure using the routine CRYSOL does not fit the data but is shifted toward larger scattering vectors q, indicating that the crystal structure is too small. This is also reflected in the pair distribution functions P(r) shown in the right panel of Figure 2. The P(r) function obtained from the experimental data extends to much higher distances than the P(r) function simulated based on the crystal structure. The reason for the apparent mismatch lies in the presence of a detergent belt around the PSI monomer. If the SAXS curve is calculated for PSI and a surrounding detergent belt (see red line in Figure 2), the data are well fitted except for a distinct peak at a q value of about 0.2 Å^{-1}, which is due to free micelles of detergent molecules. The latter finding reveals that in the case of a membrane protein like PSI, the detergent belt has to be considered when investigating its solution structure by SAXS. However, SAXS does not provide a possibility to investigate the solution structures of a membrane protein and of its detergent belt separately, so that SANS has to be employed in the next step.

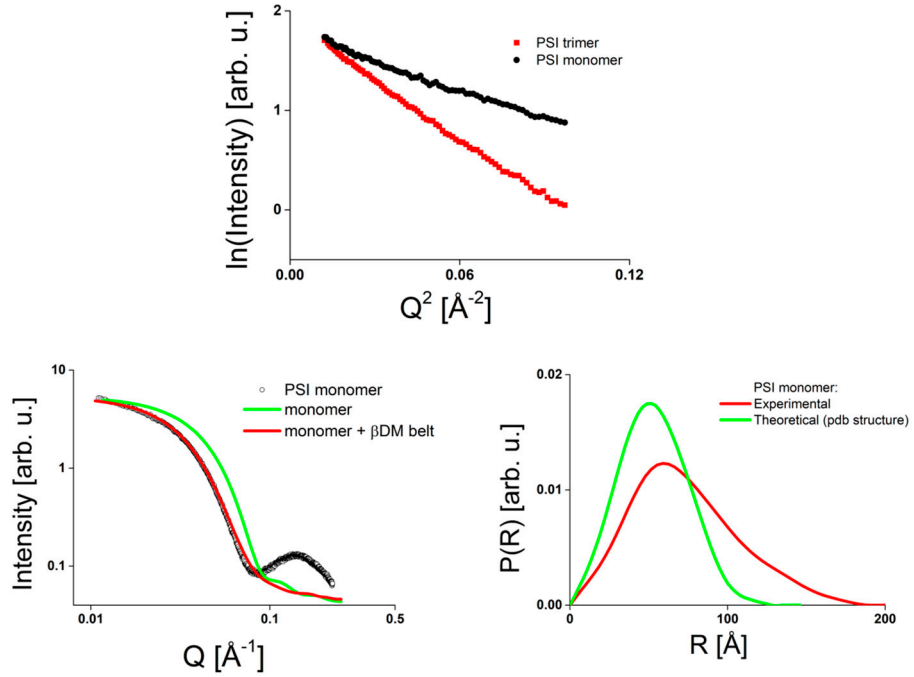

Figure 2. Photosystem I (PSI) SAXS data in comparison to the crystal structure: (**Upper**) Panel: SAXS curves of solubilized PSI in monomeric (black) and trimeric form (red) shown as Guinier plots at small q values. (**Lower Left**) Panel: Experimental SAXS curves (black dots) with fits based on the crystal structure of monomeric PSI only (green) and assuming a detergent belt around PSI (red). (**Lower Right**) Panel: Normalized pair distance distribution (P(r)) functions derived from the experimental SAXS data (red) and from the PSI crystal structures (green) by inverse Fourier transform. Graphics taken from Golub et al., 2017 [62] with permission.

2.1.3. PSI as Example for a Membrane Protein Studied by SANS

As pointed out above, SANS is a method largely equivalent to SAXS. However, one of the major advantages of SANS is the possibility of contrast matching. That is, the effective SLD of the solvent can be tuned by varying its D_2O content so that it matches, for example, either the SLD of the protein or of the detergent part of a protein–detergent complex. As a result, either the protein or the detergent is expected to become "invisible" in a SANS experiment, thus highlighting the remaining component of a protein–detergent complex selectively. The same approach can be used for any component of a protein complex, provided that it can be selectively deuterated. Making use of the different SLDs, a D_2O content of 5% matches the longer detergent tails only so that resulting SANS data largely reflect to the protein contribution only (see, e.g., [63]).

We now consider the structural information that can be derived for trimeric PSI from the SANS data with detergent match. SANS data of PSI in a βDM-containing buffer are shown in Figure 3 for a contrast of 5% D_2O, the data are taken from Kölsch et al., 2020 [15]. The data exhibit a typical (linear) Guinier behavior at small Q values (see right panel in Figure 3) and are thus virtually free of aggregation, which may affect the spectroscopic properties of a photosystem [64–66]. A radius of gyration Rg of 75.2 ± 3 can be determined from the slope of the Guinier plot. The latter value is about 4 Å smaller than those reported earlier by Le et al. [37] (see Table 2 for a comparison of Rg values of the present and other studies). For comparison, the right panel of Figure 3 also shows data obtained from the PSI crystal structure (black dots) corresponding to Rg of 68.2 Å. The latter value is roughly 10% smaller than the experimental ones reported here and suggests that PSI in solution at physiological temperature is slightly expanded compared with the crystal structure. A similar expansion in the order of 10% of the Rg value was reported by Midtgaard et al. [67] for plant PSI using fully deuterated "invisible" detergent. SANS data of PSI in 100%

D_2O (see blue dots in Figure 3) yield an Rg of 79 Å ± 3, which corresponds to the whole PSI–detergent complex.

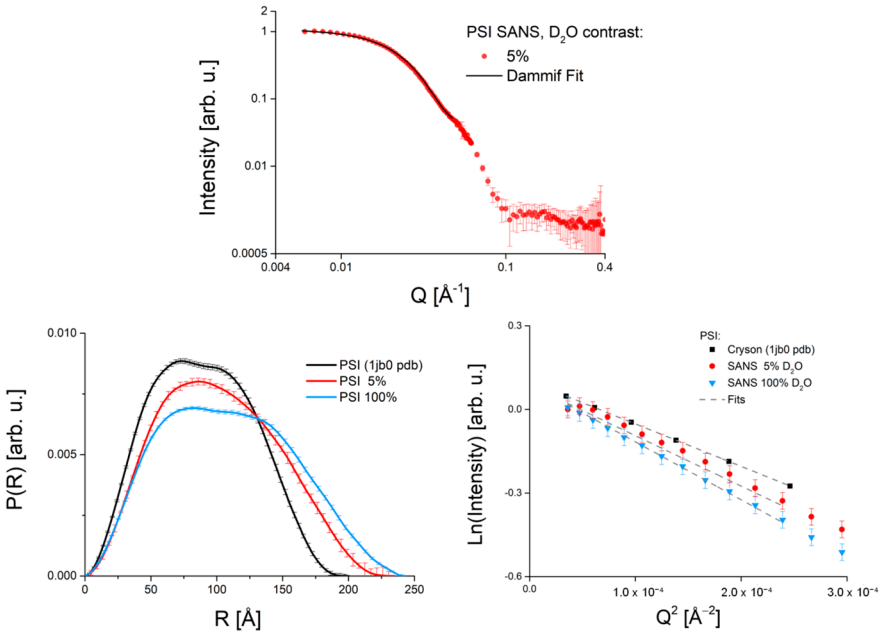

Figure 3. (**Upper**) panel: SANS data of the PSI–βDM complex at a contrast of 5%. Data are taken from Kölsch et al., 2020 [15]. (**Lower left**) panel: Pair distance distribution function P(R) of the PSI–βDM complex in 5% D_2O (red line) and 100% D_2O (blue line). For comparison, the P(R) function corresponding to the crystal structure of PSI (pdb code 1jb0 [10]) is also shown. (**Lower right**) panel: Guinier plots of the PSI–βDM complex. Color code is the same as in the left panel.

The pair distance distribution function, P(R), calculated from the SANS data measured at a contrast of 5% D_2O via IFT using Gnom is shown in the left panel of Figure 3 and compared with the curve determined from the crystal structure (pdb code 1jb0 [10]). As indicated by the larger radius of gyration Rg above, the experimental P(R) function of PSI in buffer solution appears to be broader and shifted to larger distances than that of the PSI crystal. Finally, the P(R) function of PSI in 100% D_2O extends to much higher distances, because it corresponds to the whole PSI–detergent complex, see below.

The low-resolution structure of PSI in buffer solution was derived from the SANS data measured at a contrast of 5% D_2O using the Dammif routine (see Section 2). The corresponding fit of the SANS data is shown in Figure 3 as a full black line. The latter fit function describes the SANS data at both contrasts employed. The result of the ab initio reconstruction of the PSI solution structure is shown by grey spheres and compared with the crystal structure of trimeric PSI in Figure 4. As already indicated by the experimental Rg value above, the modeled structure appears to be expanded, especially in the regions of hydrophobic surfaces and in the region of membrane-extrinsic proteins, but more similar to the crystal structure than that of Le et al. [37]. A contraction of photosystems along the membrane plane upon freezing has been shown by the comparison of crystal structures measured at room temperature to crystal structures measured at cryogenic temperatures [13,68]. However, this contraction observed for crystals leads to a less pronounced change in the radius than reported here for the solution structure of PSI. An expansion of PSI in solution is also generally in line with recent cryo-EM studies [15], although of smaller extent than reported here for physiological temperatures. Another factor affecting the size of PSI in solution may be conformational flexibility, which is enhanced by hydration of PSI [69] and PSII at elevated temperatures [70] but also depends strongly on temperature itself [25,71]. In summary, the latter observations indicate that temperature and solvent/hydration may affect the structure of PSI in solution under physiological conditions. This may mean that the close packing of protein residues in

a crystal does not allow a protein to sample all potential conformational substates at physiological temperatures, while cryo-EM may not reflect all possible conformations of the protein because of the low temperatures employed.

Table 2. Comparison of parameters R_g and D_{max} obtained at different contrasts in this work with literature values. Values of this study are highlighted in yellow; values obtained from crystal structures are marked in grey.

	PDB	Reference	Guinier R_g (Å)	R_g (Å) from IFT (Gnom)	D_{max} (Å)
SANS PSI 5% D_2O		Figure 3	75.2 ± 3	75.8 ± 3	230 ± 10
SANS PSI 100% D_2O		Figure 3 and Figure 5	79 ± 3	83 ± 3	245 ± 10
SAXS PSI monomer		[62]	58 ± 4	54 ± 2	185 ± 10
SAXS PSI trimer		[62]	78 ± 2	79.8 ± 2	250 ± 15
PSI *T. elongatus* (trimer) crystal structure	1JB0	[10]	68.2	68.28	200
SANS PSI 18% D_2O		[37]	77.9 ± 2.86	75.9 ± 0.1	215 ± 10
SANS PSI 100% D_2O		[37]	94.9 ± 2.32	93.1 ± 1.1	280 ± 10
Plant PSI (monomer) crystal structure	5L8R	[11]	50.3	50.3	173.8
Plant PSI d-βDM 100% D_2O (monomer)		[67]		55.2 ± 0.2	199 ± 5
PSI *T. elongatus* (trimer) Cryo-EM	6TRD	[15]	68.15	68.51	205

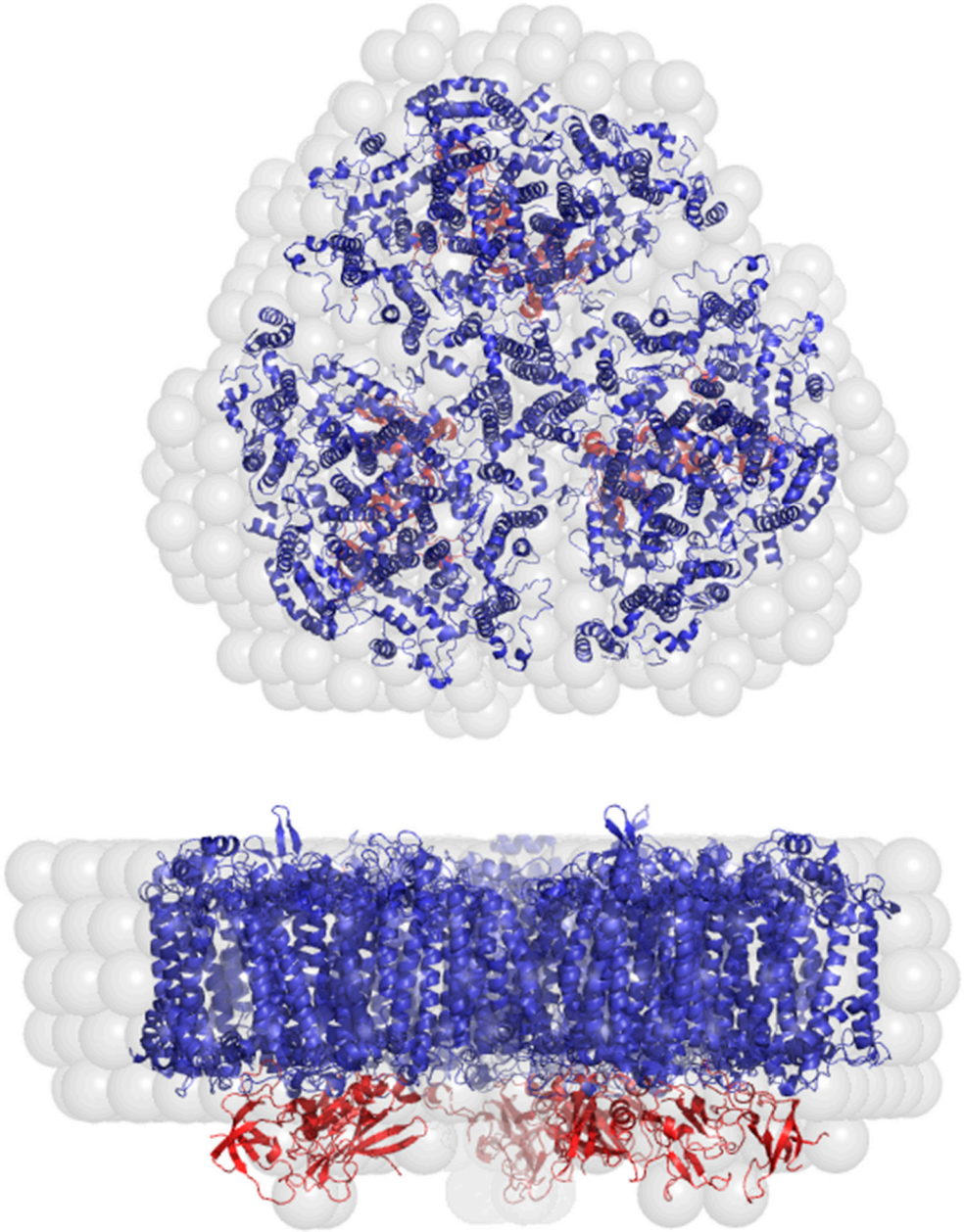

Figure 4. Top view (**upper panel**) and lateral view (**lower panel**) of the structure of PSI reconstituted based on the 5% D_2O contrast matched SANS data shown in Figure 3 using the Dammif software tool (grey spheres). For the comparison, the membrane-intrinsic and membrane-extrinsic subunits of the PSI crystal structure are shown in blue and red, respectively (pdb code 1jb0 [10]).

3. Solution Structure of the PSI–βDM Complex and Its Detergent Belt

The solution structure of the whole PSI–βDM complex was investigated by SANS experiments using a contrast of 100% D_2O (see Figure 5). Before we proceed with the solution structure of the PSI–detergent complex determined from the SANS data, we recall that our earlier SAXS data [62] indicated the presence of free detergent micelles in the preparation, which were visible as a distinct peak at about 0.17 $Å^{-1}$ corresponding to a small spherical particle with an average size of only about 35–40 Å. The latter peak is not separately visible in the SANS data presented here but had to be considered in a simultaneous analysis of PSII SANS and SAXS data [63]. In analogy, we use the shape of free detergent micelles derived from SAXS data before [62] to fit the SANS data of the PSI–detergent complex in this study (Figure 5).

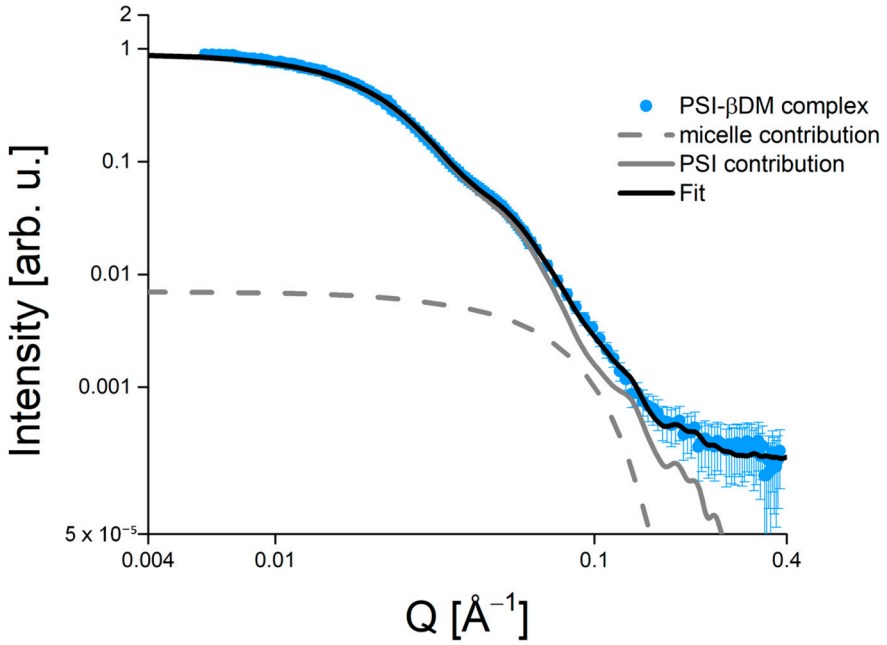

Figure 5. Fit of the PSI SANS data (blue points) measured at 100% D_2O: The fit function (black line) is composed of (i) the reconstituted structure of the PSI trimer (gray line) and (ii) a contribution of free βDM vesicles (dotted gray line).

Accordingly, the fit of the SANS data of the PSI–detergent complex shown in Figure 5 is a linear superposition of two components: (1) solution structure of the protein–detergent complex reconstructed using Dammif and (2) a spherical core shell representing the contribution of free micelles as determined by Golub et al. [62]. The analysis using Dammif was performed only for Q values smaller than 0.07 Å^{-1}, where the contribution of the free βDM micelles to the experimental scattering data is weak and structureless (see Figure 5). The structure of the PSI–detergent complex derived from the SANS data is compared to the PSI structure obtained at 5% D_2O above in Panel A of Figure 6. The difference between the two contrasts allows us to reconstruct the detergent belt surrounding PSI. A closer inspection of this plot clearly reveals that there is an additional structure surrounding the PSI trimer, which is mainly located at its hydrophobic surfaces, i.e., at those surfaces that are surrounded by lipid molecules when PSI is embedded in the thylakoid membrane. The size of this additional structure is in the range of 10–15 Å, which is very close to the length of a single βDM detergent molecule. This finding corroborates the conclusion that trimeric PSI is surrounded by a monolayer of detergent molecules at its hydrophobic surface. At this point, we recall that Le et al. [37] reported an Rg value for the PSI–detergent complex, which is about 16 Å larger than determined here (see Table 2). This was most probably the reason to propose detergent layers within the PSI trimer, which are not necessary within our model.

In the two lower panels of Figure 6, the solution structure obtained using Dammif is compared with a model comprising the crystal structure of trimeric PSI and a simulated monolayer of detergent molecules. Assuming the closest packing of detergent molecules, the simulation yields a value of 1530 (170 rows with 9 βDM molecules in a row) βDM molecules bound in the PSI–detergent complex. This finding is in general agreement with our earlier SAXS data [62] and with previous studies on protein–detergent interactions, which typically reveal a ring-like monolayer of detergent molecules bound to membrane proteins [16,72–74].

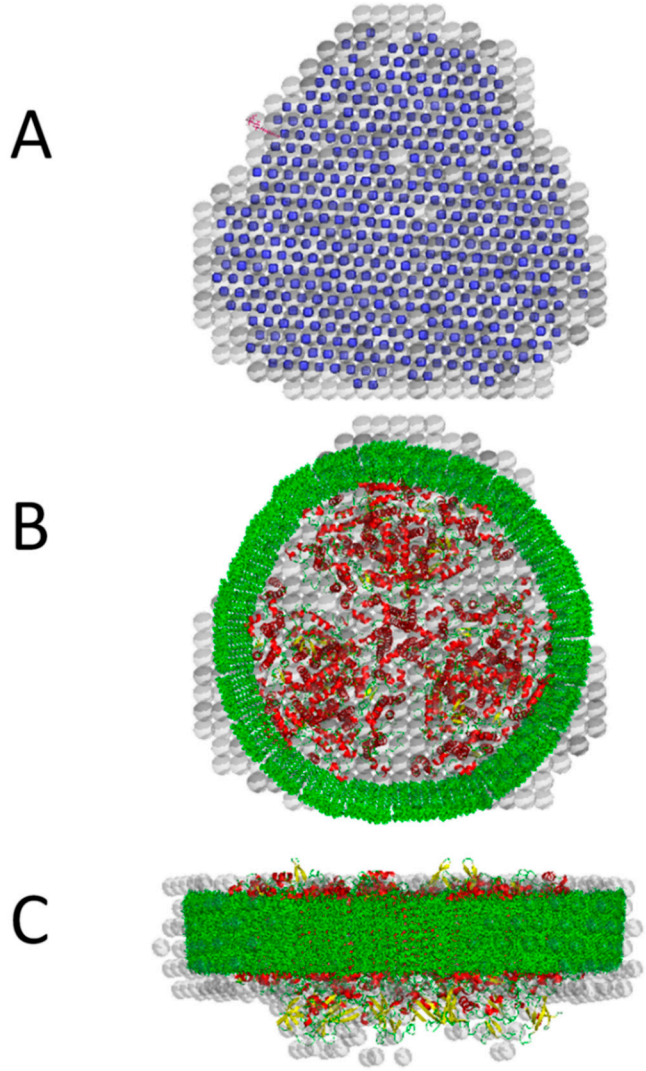

Figure 6. Panel (**A**): Comparison of the ab initio reconstructions of the solution structures of PSI from SANS data with detergent match at 5% D_2O taken from Figure 3 (blue dots) and of the PSI–detergent complex from SANS data without detergent match at 100% D_2O (grey spheres, for easy of inspection spheres are shown with 80% transparency). Panels (**B**,**C**) Top view (**B**) and lateral view (**C**) of the crystal structure of PSI (pdb code 1jb0 [10]) and the solution structure (grey spheres) produced by Dammif based on the SANS data of the PSI–detergent complex at a contrast of 100% D_2O. The difference can be accounted for by a monolayer of detergent molecules (see green structures).

4. Comparison of Different PSI Preparations

Our SANS data at 100% D_2O, as well as our SAXS data, suggest that the detergent belt contains approximately 1500 molecules of βDM. However, a previous SANS experiment combined with molecular dynamics simulation suggested a belt containing 800 molecules of D_2O [37]. Geometric calculations suggested 1200 molecules of βDM [74]. To test whether there is a variance in the size of the detergent belt with preparation protocol, we measured three different isolations of PSI. The first one (PSI A, as used above) was measured in 20 mM MES buffer pH/pD 6.4, 50 mM $MgSO_4$ and 0.02% βDM, as was also used to characterize the detergent belt in [74]. A second isolation (PSI B) was measured in the presence of 25 mM Tricine pH/pD 8.0, 25 mM NaCl and 0.02% βDM. We could not reproduce the buffer conditions used in Le et al. (MES pH 6.5, 0.03% βDM without additional salt) [37], as our PSI preparations crystallize quickly under these conditions [52]. For a third measurement (PSI C), we wanted to know if the detergent concentration during solubilization of PSI influences the shape of the protein–detergent complex. Increasing

the detergent concentration during solubilization affects the oligomeric state of PSII [75]. Therefore, we isolated a batch of PSI by the addition of four times as much detergent during the thylakoid membrane solubilization (2% βDM) and measured it under the conditions from the first isolation. The SANS data for the three PSI preparations are shown in Figure 7 for both contrasts of 5% and 100% D_2O. The fit functions shown in Figures 2 and 5 are also provided in Figure 7 for comparison. The data prove that all preparations of PSI yield similar solution structures for the protein–detergent complex as well as for PSI itself. Furthermore, the data show that all samples are monodisperse and virtually free of aggregation. We conclude that neither changes in pH nor the concentration of detergent during the isolation cause a significant deviation in the structure of the protein–detergent complex.

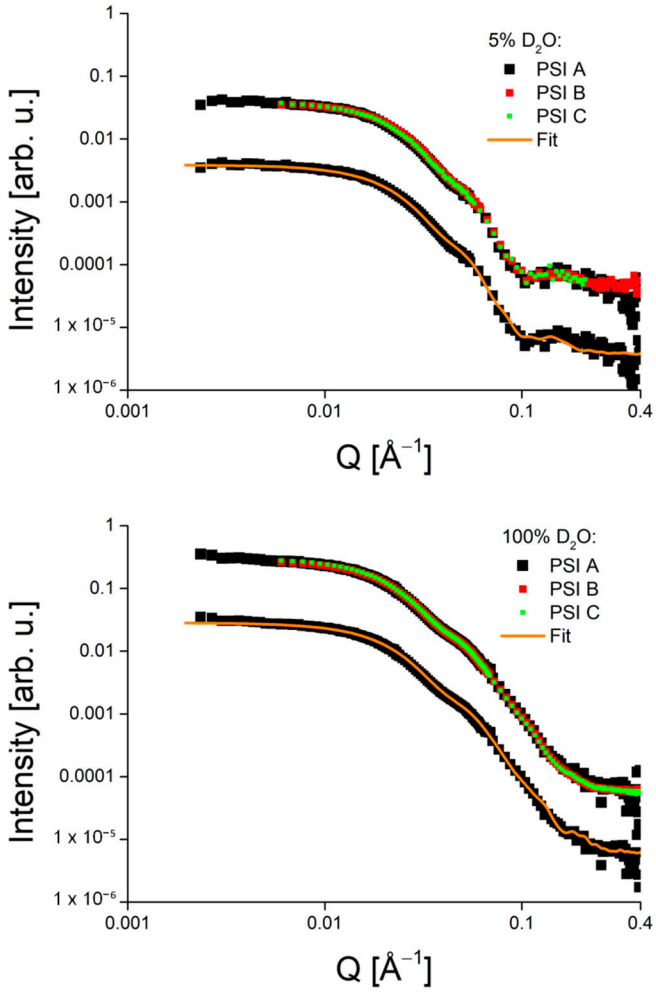

Figure 7. Comparison of SANS data of three different preparations of the PSI–βDM complex PSI A, B, and C (see text), respectively, in 5% (upper panel) and 100% D_2O (lower panel). The data fit produced by Dammif is shown for one of the data sets in each panel as a solid orange line. For ease of inspection, the latter data set is given an artificial offset of one order of magnitude.

5. Conclusions

In this short review, we have presented selected applications for SANS and SAXS as powerful experimental tool to study protein structures in aqueous solution at physiological temperatures using the photosynthetic pigment–protein complexes phycocyanin (PC) and Photosystem I (PSI) as model systems. We have demonstrated that SANS and SAXS have a number of useful applications, including: (i) verification of the oligomeric state of proteins, (ii) check for aggregation, (iii) investigation of deviations of the solution structure from high-resolution crystal or electron microscopy structures, and (iv) studies of the structure

of the inherently structurally heterogeneous detergent belt around solubilized membrane proteins.

Especially, we have investigated the solution structure of trimeric PSI of *T. elongatus* solubilized in ßDM using SANS with contrast variation. The low-resolution solution structure of PSI appears to be similar to the crystal structure, but slightly expanded with a radius of gyration of about 75 Å in solution compared with about 68 Å in the crystal structure. The extent of protein expansion in solution reported here is similar to that found for plant PSI using "invisible" deuterated detergent by Midtgaard et al. [67]. An expansion of PSI was also reported for crystals at room temperature [13,68] as well as in solution in recent cryo-EM studies [15], indicating effects of temperature and solvent/hydration on the protein structure. A possible explanation is the influence of molecular dynamics allowing the protein to sample further conformational substates depending on hydration [69,70] and at physiological temperatures [25,71]. SANS experiments with and without detergent match were used to study the PSI–detergent complex. It can be concluded that Photosystem I is surrounded by a monolayer of detergent molecules under proper solubilization conditions. The structural studies of PSI in solution using SANS/SAXS measurements are also of significant importance with respect to other membrane protein–detergent complexes (e.g., PSII).

Author Contributions: Conceptualization, M.G., A.K., A.Z. and J.P.; methodology, M.G., A.F. and J.P.; software, M.G.; validation, A.Z. and J.P.; formal analysis, M.G.; investigation, M.G.; resources, A.Z. and J.P.; data curation, M.G.; writing—original draft preparation, M.G., A.K., A.F., A.Z. and J.P.; writing—review and editing, J.P.; visualization, M.G.; supervision, A.Z. and J.P.; project administration, A.Z. and J.P.; funding acquisition, A.Z. and J.P. All authors have read and agreed to the published version of the manuscript.

Funding: Financial support by the Estonian Research Council (Grants PRG 539 and SLOKT 12026 T) is gratefully acknowledged. A.Z. and A.K. greatly appreciate financial support by the Deutsche Forschungsgemeinschaft (DFG, German Research Foundation) under Germany´s Excellence Strategy—EXC 2008/1 and EXC 314/2–390540038 (Gefördert durch die Deutsche Forschungsgemeinschaft (DFG) im Rahmen der Exzellenzstrategie des Bundes und der Länder—EXC 2008/1 und EXC 314/2–390540038) and Sfb1078 (Humboldt Universität Berlin), TP A5 (Zouni/Dobbek). Financial support by the Federal Ministry for Education and Research (BMBF) within the project 031B0557A+B (Biotechnology 2020) is highly acknowledged.

Data Availability Statement: The datasets generated during and/or analyzed in the present study are available from the corresponding author on reasonable request.

Acknowledgments: A part of this work is based on SANS experiments performed at the KWS-1 instrument operated by Jülich Centre for Neutron Science (JCNS) at the Heinz Maier-Leibnitz Zentrum (MLZ), Garching, Germany. We thank JCNS and MLZ for the allocation of beamtime.

Conflicts of Interest: The authors declare that there is no conflict of interest.

References

1. Nelson, N.; Yocum, C.F. Structure and function of photosystems I and II. *Annu. Rev. Plant Biol.* **2006**, *57*, 521–565. [CrossRef]
2. Müh, F.; Zouni, A. Light-induced water oxidation in Photosystem II. *Front. Biosci.* **2011**, *16*, 3072–3132. [CrossRef] [PubMed]
3. Lambreva, M.D.; Russo, D.; Polticelli, F.; Scognamiglio, V.; Antonacci, A.; Zobnina, V.; Campi, G.; Rea, G. Structure/function/dynamics of Photosystem II plastoquinone binding sites. *Curr. Protein Pept. Sci.* **2014**, *15*, 285–295. [CrossRef] [PubMed]
4. Najafpour, M.M.; Renger, G.; Hołyńska, M.; Moghaddam, A.N.; Aro, E.-M.; Carpentier, R.; Nishihara, H.; Eaton-Rye, J.J.; Shen, J.-R.; Allakhverdiev, S.I. Manganese Compounds as Water-Oxidizing Catalysts: From the Natural Water-Oxidizing Complex to Nanosized Manganese Oxide Structures. *Chem. Rev.* **2016**, *116*, 2886–2936. [CrossRef]
5. Golbeck, J.H. *Photosystem I, the Light-Driven Plastocyanin: Ferredoxin Oxidoreductase*, 1st ed.; Springer: Dordrecht, The Netherlands, 2006; Volume 24, p. 713.
6. Mershin, A.; Matsumoto, K.; Kaiser, L.; Yu, D.; Vaughn, M.; Nazeeruddin, K.; Bruce, B.D.; Graetzel, M.; Zhang, S. Self-assembled photosystem-I biophotovoltaics on nanostructured TiO2 and ZnO. *Sci. Rep.* **2012**, *2*, 234. [CrossRef] [PubMed]

7. Gorka, M.; Schartner, J.; van der Est, A.; Rogner, M.; Golbeck, J.H. Light-mediated hydrogen generation in Photosystem I: Attachment of a naphthoquinone-molecular wire-Pt nanoparticle to the A1A and A1B sites. *Biochemistry* **2014**, *53*, 2295–2306. [CrossRef] [PubMed]
8. Feifel, S.C.; Lokstein, H.; Hejazi, M.; Zouni, A.; Lisdat, F. Unidirectional photocurrent of Photosystem I on pi-system-modified graphene electrodes: Nanobionic approaches for the construction of photobiohybrid systems. *Langmuir* **2015**, *31*, 10590–10598. [CrossRef] [PubMed]
9. Stieger, K.R.; Feifel, S.C.; Lokstein, H.; Hejazi, M.; Zouni, A.; Lisdat, F. Biohybrid architectures for efficient light-to-current conversion based on photosystem I within scalable 3D mesoporous electrodes. *J. Mater. Chem. A* **2016**, *4*, 17009–17017. [CrossRef]
10. Jordan, P.; Fromme, P.; Witt, H.T.; Klukas, O.; Saenger, W.; Krauss, N. Three-dimensional structure of cyanobacterial Photo-system I at 2.5 A resolution. *Nature* **2001**, *411*, 909–917. [CrossRef]
11. Mazor, Y.; Borovikova, A.; Caspy, I.; Nelson, N. Structure of the plant photosystem I supercomplex at 2.6 Å resolution. *Nat. Plants* **2017**, *3*, 17014. [CrossRef]
12. Gisriel, C.; Coe, J.; Letrun, R.; Yefanov, O.M.; Luna-Chavez, C.; Stander, N.E.; Lisova, S.; Mariani, V.; Kuhn, M.; Aplin, S.; et al. Membrane protein megahertz crystallography at the European XFEL. *Nat. Commun.* **2019**, *10*, 5021. [CrossRef]
13. Young, I.D.; Ibrahim, M.; Chatterjee, R.; Gul, S.; Fuller, F.D.; Koroidov, S.; Brewster, A.S.; Tran, R.; Alonso-Mori, R.; Kroll, T.; et al. Structure of photosystem II and substrate binding at room temperature. *Nat. Cell Biol.* **2016**, *540*, 453–457. [CrossRef] [PubMed]
14. Kern, J.; Chatterjee, R.; Young, I.D.; Fuller, F.D.; Lassalle, L.; Ibrahim, M.; Gul, S.; Fransson, T.; Brewster, A.S.; Alonso-Mori, R.; et al. Structures of the intermediates of Kok's photosynthetic water oxidation clock. *Nat. Cell Biol.* **2018**, *563*, 421–425. [CrossRef]
15. Kölsch, A.; Radon, C.; Golub, M.; Baumert, A.; Bürger, J.; Mielke, T.; Lisdat, F.; Feoktystov, A.; Pieper, J.; Zouni, A.; et al. Current limits of structural biology: The transient interaction between cytochrome c and photosystem I. *Curr. Res. Struct. Biol.* **2020**, *2*, 171–179. [CrossRef]
16. Le Maire, M.; Champeil, P.; Møller, J.V. Interaction of membrane proteins and lipids with solubilizing detergents. *Biochim. Biophys. Acta (BBA) Biomembr.* **2000**, *1508*, 86–111. [CrossRef]
17. Seddon, A.M.; Curnow, P.; Booth, P.J. Membrane proteins, lipids and detergents: Not just a soap opera. *Biochim. Biophys. Acta (BBA) Biomembr.* **2004**, *1666*, 105–117. [CrossRef] [PubMed]
18. Mo, Y.; Lee, B.K.; Ankner, J.F.; Becker, J.M.; Heller, W.T. Detergent-associated solution conformations of helical and beta-barrel membrane proteins. *J. Phys. Chem. B* **2008**, *112*, 13349–13354. [CrossRef]
19. Cardoso, M.B.; Smolensky, D.; Heller, W.T.; O'Neill, H. Insight into the Structure of Light-Harvesting Complex II and Its Stabilization in Detergent Solution. *J. Phys. Chem. B* **2009**, *113*, 16377–16383. [CrossRef]
20. Jacques, D.A.; Trewhella, J. Small-angle scattering for structural biology-Expanding the frontier while avoiding the pitfalls. *Protein Sci.* **2010**, *19*, 642–657. [CrossRef]
21. Breyton, C.; Gabel, F.; Lethier, M.; Flayhan, A.; Durand, G.; Jault, J.-M.; Juillan-Binard, C.; Imbert, L.; Moulin, M.; Ravaud, S.; et al. Small angle neutron scattering for the study of solubilised membrane proteins. *Eur. Phys. J. E* **2013**, *36*, 1–16. [CrossRef] [PubMed]
22. Kikhney, A.G.; Svergun, D.I. A practical guide to small angle X-ray scattering (SAXS) of flexible and intrinsically disordered proteins. *FEBS Lett.* **2015**, *589*, 2570–2577. [CrossRef] [PubMed]
23. Kuhn, P.; Pieper, J.; Kaminskaya, O.; Eckert, H.-J.; Lechner, R.E.; Shuvalov, V.; Renger, G. Reaction pattern of Photosystem II: Oxidative water cleavage and protein flexibility. *Photosynth. Res.* **2005**, *84*, 317–323. [CrossRef]
24. Pieper, J.; Renger, G. Protein dynamics investigated by neutron scattering. *Photosynth. Res.* **2009**, *102*, 281–293. [CrossRef] [PubMed]
25. Pieper, J.; Trapp, M.; Skomorokhov, A.; Natkaniec, I.; Peters, J.; Renger, G. Temperature-dependent vibrational and conformational dynamics of Photosystem II membrane fragments from spinach investigated by elastic and inelastic neutron scattering. *Biochim. Biophys. Acta* **2012**, *1817*, 1213–1219. [CrossRef]
26. Golub, M.; Rusevich, L.; Irrgang, K.-D.; Pieper, J. Rigid versus Flexible Protein Matrix: Light-Harvesting Complex II Exhibits a Temperature-Dependent Phonon Spectral Density. *J. Phys. Chem. B* **2018**, *122*, 7111–7121. [CrossRef]
27. Nagy, G.; Garab, G.; Pieper, J. Neutron scattering in photosynthesis research. In *Contemporary Problems of Photosynthesis*; Al-lakhverdiev, S., Rubin, A.B., Shuvalov, V.A., Eds.; Institute of Computer Science: Izhevsk, Russia, 2014; Volume 1, pp. 69–121.
28. Tiede, D.M.; Thiyagarjan, P. Characterization of photosynthetic supramolecular assemblies using small angle neutron scat-tering. In *Biophysical Techniques in Photosynthesis*; Amesz, J., Hoff, A.J., Eds.; Springer: Dordrecht, The Netherlands, 1996; Volume 3, pp. 375–390.
29. Kirkensgaard, J.J.K.; Holm, J.K.; Larsen, J.K.; Posselt, D. Simulation of small-angle X-ray scattering from thylakoid membranes. *J. Appl. Cryst.* **2009**, *42*, 649–659. [CrossRef]
30. Nagy, G.; Posselt, D.; Kovács, L.; Holm, J.K.; Szabó, M.; Ughy, B.; Rosta, L.; Peters, J.; Timmins, P.; Garab, G. Reversible membrane reorganizations during photosynthesis in vivo: Revealed by small-angle neutron scattering. *Biochem. J.* **2011**, *436*, 225–230. [CrossRef]
31. Liberton, M.; Page, L.E.; O'Dell, W.B.; O'Neill, H.; Mamontov, E.; Urban, V.S.; Pakrasi, H.B. Organization and Flexibility of Cyanobacterial Thylakoid Membranes Examined by Neutron Scattering. *J. Biol. Chem.* **2013**, *288*, 3632–3640. [CrossRef] [PubMed]
32. Jakubauskas, D.; Kowalewska, Ł.; Sokolova, A.V.; Garvey, C.J.; Mortensen, K.; Jensen, P.E.; Kirkensgaard, J.J.K. Ultrastructural modeling of small angle scattering from photosynthetic membranes. *Sci. Rep.* **2019**, *9*, 19405. [CrossRef] [PubMed]

33. Tiede, D.M.; Littrell, K.; Marone, P.A.; Zhang, R.; Thiyagarjan, P. Solution structure of a biological bimolecular electron transfer complex: Characterization of the photosynthetic reaction center-cytochrome C2 protein complex by small angle neutron scattering. *J. Appl. Crystallogr.* **2000**, *33*, 560–564. [CrossRef]
34. O'Neill, H.; Heller, W.T.; Helton, K.E.; Urban, V.S.; Greenbaum, E. Small-Angle X-ray Scattering Study of Photosystem I−Detergent Complexes: Implications for Membrane Protein Crystallization. *J. Phys. Chem. B* **2007**, *111*, 4211–4219. [CrossRef] [PubMed]
35. Slowik, D.; Rossmann, M.; Konarev, P.V.; Irrgang, K.D.; Saenger, W. Structural investigation of PsbO from plant and cyano-bacterial Photosystem II. *J. Mol. Biol.* **2011**, *407*, 125–137. [CrossRef]
36. Tang, K.-H.; Blankenship, R.E. Neutron and light scattering studies of light-harvesting photosynthetic antenna complexes. *Photosynth. Res.* **2011**, *111*, 205–217. [CrossRef]
37. Le, R.K.; Harris, B.J.; Iwuchukwu, I.J.; Bruce, B.D.; Cheng, X.; Qian, S.; Heller, W.T.; O'Neill, H.; Frymier, P.D. Analysis of the solution structure of Thermosynechococcus elongatus Photosystem I in n-dodecyl-beta-D-maltoside using small-angle neutron scattering and molecular dynamics simulation. *Arch. Biochem. Biophys.* **2014**, *550*, 50–57. [CrossRef]
38. Golub, M.; Moldenhauer, M.; Schmitt, F.-J.; Feoktystov, A.; Mändar, H.; Maksimov, E.; Friedrich, T.; Pieper, J. Solution Structure and Conformational Flexibility in the Active State of the Orange Carotenoid Protein: Part I. Small-Angle Scattering. *J. Phys. Chem. B* **2019**, *123*, 9525–9535. [CrossRef] [PubMed]
39. Golub, M.; Moldenhauer, M.; Schmitt, F.J.; Lohstroh, W.; Maksimov, E.G.; Friedrich, T.; Pieper, J. Solution structure and conformational flexibility in the active state of the Orange Carotenoid Protein. Part II: Quasielastic neutron scattering. *J. Phys. Chem. B* **2019**, *123*, 9536–9545. [CrossRef] [PubMed]
40. Guinier, A.; Fournet, G. *Small-Angle Scattering of X-rays*; John Wiley and Sons: New York, NY, USA, 1955.
41. Svergun, D. Determination of the regularization parameter in indirect-transform methods using perceptual criteria. *J. Appl. Cryst.* **1992**, *25*, 495–503. [CrossRef]
42. Konarev, P.V.; Volkov, V.V.; Sokolova, A.V.; Koch, M.H.J.; Svergun, D.I. PRIMUS: A Windows PC-based system for small-angle scattering data analysis. *J. Appl. Cryst.* **2003**, *36*, 1277–1282. [CrossRef]
43. Franke, D.; Svergun, D.I. DAMMIF, a program for rapid ab-Initio shape determination in small-angle scattering. *J. Appl. Crystallogr.* **2009**, *42*, 342–346. [CrossRef]
44. Petoukhov, M.V.; Franke, D.; Shkumatov, A.V.; Tria, G.; Kikhney, A.G.; Gajda, M.; Gorba, C.; Mertens, H.D.; Konarev, P.V.; Svergun, D.I. New developments in the ATSAS program package for small-angle scattering data analysis. *J. Appl. Crystallogr.* **2012**, *45*, 342–350. [CrossRef]
45. Svergun, D.I.; Barberato, C.; Koch, M.H.J. CRYSOL—A program to evaluate X-ray solution scattering of biological macromolecules form atomic coordinates. *J. Appl. Crystallogr.* **1995**, *28*, 768–773. [CrossRef]
46. Svergun, D.I.; Richard, S.; Koch, M.H.J.; Sayers, Z.; Kuprin, S.; Zaccai, G. Protein hydration in solution: Experimental obser-vation by x-ray and neutron scattering. *Proc. Natl. Acad. Sci. USA* **1998**, *95*, 2267–2272. [CrossRef]
47. DeLano, W.L. *PyMOL Molecular Graphics System 0.99*; Schrödinger, Inc: New York, NY, USA, 2006.
48. Jacrot, B. The study of biological structures by neutrons cattering from solution. *Rep. Prog. Phys.* **1976**, *39*, 911–953. [CrossRef]
49. Kikhney, A.G.; Borges, C.R.; Molodenskiy, D.S.; Jeffries, C.M.; Svergun, D.I. SASBDB: Towards an automatically curated and validated repository for biological scattering data. *Protein Sci.* **2020**, *29*, 66–75. [CrossRef] [PubMed]
50. Feoktystov, A.V.; Frielinghaus, H.; Di, Z.; Jaksch, S.; Pipich, V.; Appavou, M.-S.; Babcock, E.; Hanslik, R.; Engels, R.; Kemmerling, G.; et al. KWS-1 high-resolution small-angle neutron scattering instrument at JCNS: Current state. *J. Appl. Cryst.* **2015**, *48*, 61–70. [CrossRef]
51. Frielinghaus, H.; Feoktystov, A.; Berts, I.; Mangiapia, G. KWS-1: Small-angle scattering diractometer. *J. Large Scale Res. Facil.* **2015**, *1*, 1–4. [CrossRef]
52. Kölsch, A.; Hejazi, M.; Stieger, K.R.; Feifel, S.C.; Kern, J.F.; Müh, F.; Lisdat, F.; Lokstein, H.; Zouni, A. Insights into the binding behavior of native and non-native cytochromes to photosystem I from Thermosynechococcus elongatus. *J. Biol. Chem.* **2018**, *293*, 9090–9100. [CrossRef]
53. Kern, J.; Loll, B.; Luneberg, C.; DiFiore, D.; Biesiadka, J.; Irrgang, K.D.; Zouni, A. Purification, characterisation and crystalli-sation of Photosystem II from Thermosynechococcus elongatus cultivated in a new type of photobioreactor. *Biochim. Biophys. Acta* **2005**, *1706*, 147–157. [CrossRef]
54. Fromme, R.; Ishchenko, A.; Metz, M.; Chowdhury, S.R.; Basu, S.; Boutet, S.; Fromme, P.; White, T.A.; Barty, A.; Spence, J.C.H.; et al. Serial femtosecond crystallography of soluble proteins in lipidic cubic phase. *IUCrJ* **2015**, *2*, 545–551. [CrossRef]
55. Conrad, C.E.; Basu, S.E.; James, D.; Wang, D.; Schaffer, A.; Roy-Chowdhury, S.; Zatsepin, N.A.; Aquila, A.; Coe, J.; Gati, C.; et al. A novel inert crystal delivery medium for serial femtosecond crystallography. *IUCrJ* **2015**, *2*, 421–430. [CrossRef]
56. Chen, M.; Floetenmeyer, M.; Bibby, T.S. Supramolecular organization of phycobiliproteins in the chlorophyll d -containing cyanobacterium Acaryochloris marina. *FEBS Lett.* **2009**, *583*, 2535–2539. [CrossRef]
57. Watanabe, M.; Ikeuchi, M. Phycobilisome: Architecture of a light-harvesting supercomplex. *Photosynth. Res.* **2013**, *116*, 265–276. [CrossRef] [PubMed]
58. Theiss, C.; Schmitt, F.-J.; Pieper, J.; Nganou, C.; Grehn, M.; Vitali, M.; Olliges, R.; Eichler, H.J.; Eckert, H.-J. Excitation energy transfer in intact cells and in the phycobiliprotein antennae of the chlorophyll d containing cyanobacterium Acaryochloris marina. *J. Plant Physiol.* **2011**, *168*, 1473–1487. [CrossRef]

59. Gryliuk, G.; Rätsep, M.; Hildebrandt, S.; Irrgang, K.-D.; Eckert, H.-J.; Pieper, J. Excitation energy transfer and electron-vibrational coupling in phycobiliproteins of the cyanobacterium Acaryochloris marina investigated by site-selective spectroscopy. *Biochim. Biophys. Acta (BBA) Bioenerg.* **2014**, *1837*, 1490–1499. [CrossRef]
60. Pieper, J.; Rätsep, M.; Golub, M.; Schmitt, F.-J.; Artene, P.; Eckert, H.-J. Excitation energy transfer in phycobiliproteins of the cyanobacterium Acaryochloris marina investigated by spectral hole burning. *Photosynth. Res.* **2017**, *133*, 225–234. [CrossRef]
61. Golub, M.; Combet, S.; Wieland, D.; Soloviov, D.; Kuklin, A.; Lokstein, H.; Schmitt, F.-J.; Olliges, R.; Hecht, M.; Eckert, H.-J.; et al. Solution structure and excitation energy transfer in phycobiliproteins of Acaryochloris marina investigated by small angle scattering. *Biochim. Biophys. Acta (BBA) Bioenerg.* **2017**, *1858*, 318–324. [CrossRef] [PubMed]
62. Golub, M.; Hejazi, M.; Kölsch, A.; Lokstein, H.; Wieland, D.C.F.; Zouni, A.; Pieper, J. Solution structure of monomeric and trimeric photosystem I of Thermosynechococcus elongatus investigated by small-angle X-ray scattering. *Photosynth. Res.* **2017**, *133*, 163–173. [CrossRef]
63. Golub, M.; Hussein, R.; Ibrahim, M.; Hecht, M.; Wieland, D.C.F.; Martel, A.; Machado, B.; Zouni, A.; Pieper, J. Solution Structure of the Detergent–Photosystem II Core Complex Investigated by Small-Angle Scattering Techniques. *J. Phys. Chem. B* **2020**, *124*, 8583–8592. [CrossRef] [PubMed]
64. Vasilev, S.; Irrgang, K.D.; Schrotter, T.; Bergmann, A.; Eichler, H.J.; Renger, G. Quenching of chlorophyll alpha fluorescence in the aggregates of LHCII: Steady state fluorescence and picosecond relaxation kinetics. *Biochemistry* **1997**, *36*, 7503–7512. [CrossRef]
65. Pieper, J.; Irrgang, K.-D.; Rätsep, M.; Jankowiak, R.; Schrötter, T.; Voigt, J.; Small, G.J.; Renger, G. Effects of Aggregation on Trimeric Light-Harvesting Complex II of Green Plants: A Hole-Burning Study. *J. Phys. Chem. A* **1999**, *103*, 2422–2428. [CrossRef]
66. Voigt, B.; Krikunova, M.; Lokstein, H. Influence of detergent concentration on aggregation and spectroscopic properties of light-harvesting complex II. *Photosynth. Res.* **2007**, *95*, 317–325. [CrossRef]
67. Midtgaard, S.R.; Darwish, T.A.; Pedersen, M.C.; Huda, P.; Larsen, A.H.; Jensen, G.V.; Kynde, S.A.R.; Skar-Gislinge, N.; Nielsen, A.J.Z.; Olesen, C.; et al. Invisible detergents for structure determination of membrane proteins by small-angle neutron scattering. *FEBS J.* **2017**, *285*, 357–371. [CrossRef]
68. Juers, D.H.; Matthews, B.W. Reversible lattice repacking illustrates the temperature dependence of macromolecular interac-tions. *J. Mol. Biol.* **2001**, *311*, 851–862. [CrossRef]
69. Malferrari, M.; Savitsky, A.; Mamedov, M.D.; Milanovsky, G.E.; Lubitz, W.; Möbius, K.; Semenov, A.Y.; Venturoli, G. Trehalose matrix effects on charge-recombination kinetics in Photosystem I of oxygenic photosynthesis at different dehydration levels. *Biochim. Biophys. Acta (BBA) Bioenerg.* **2016**, *1857*, 1440–1454. [CrossRef]
70. Pieper, J.; Hauß, T.; Buchsteiner, A.; Renger, G. The effect of hydration on protein flexibility in photosystem II of green plants studied by quasielastic neutron scattering. *Eur. Biophys. J.* **2008**, *37*, 657–663. [CrossRef]
71. Russo, D.; Lambreva, M.D.; Simionesco, C.A.; Sebban, P.; Rea, G. Dynamics Properties of Photosynthetic Microorganisms Probed by Incoherent Neutron Scattering. *Biophys. J.* **2019**, *116*, 1759–1768. [CrossRef]
72. Møller, J.; Le Maire, M. Detergent binding as a measure of hydrophobic surface area of integral membrane proteins. *J. Biol. Chem.* **1993**, *268*, 18659–18672. [CrossRef]
73. Pebay-Peyroula, E.; Garavito, R.M.; Rosenbusch, J.P.; Zulauf, M.A.; Timmins, P. Detergent structure in tetragonal crystals of OmpF porin. *Structure* **1995**, *3*, 1051–1059. [CrossRef]
74. Müh, F.; Zouni, A. Micelle formation in the presence of photosystem I. *Biochim. Biophys. Acta (BBA) Biomembr.* **2008**, *1778*, 2298–2307. [CrossRef]
75. Hussein, R.; Ibrahim, M.; Chatterjee, R.; Coates, L.; Müh, F.; Yachandra, V.K.; Yano, J.; Kern, J.; Dobbek, H.; Zouni, A. Opti-mizing crystal size of Photosystem II by macroseeding: Toward neutron protein crystallography. *Cryst. Growth Des.* **2018**, *18*, 85–94. [CrossRef] [PubMed]